How Is Synoptic-Scale Circulation Influenced by the Dynamics of Mesoscale Convection in Convection-Permitting Simulations over West Africa?

FRAN MORRIS,[a] JULIANE SCHWENDIKE,[a] DOUGLAS J. PARKER,[b,c] AND CAROLINE BAIN[d]

[a] *Institute for Climate and Atmospheric Science, University of Leeds, Leeds, United Kingdom*
[b] *National Centre for Climate and Atmospheric Science, University of Leeds, Leeds, United Kingdom*
[c] *NORCE Norwegian Research Centre, Bergen, Norway*
[d] *Met Office, Exeter, United Kingdom*

(Manuscript received 10 February 2022, in final form 2 February 2023, accepted 27 March 2023)

ABSTRACT: Understanding how mesoscale convection interacts with synoptic-scale circulations over West Africa is crucial for improving regional weather forecasts and developing convection parameterizations to address biases in climate models. A 10-yr pan-African convection-permitting simulation and a corresponding parameterized simulation for current-climate conditions are used to calculate the circulation budget around a synoptic region over the diurnal cycle, splitting processes that modulate circulation tendency (vorticity accumulation and vortex tilting) into diurnal mean and anomalous contributions. Dynamical fields are composited around precipitating grid cells during afternoon and overnight convection to understand how the mesoscale convection modulates synoptic-scale processes, and the composites are compared with an observational case. The dominant process modulating circulation tendency was found to be synoptic-scale vorticity accumulation, which is similar in the two simulations. The greatest difference between the simulated budgets was the tilting term. We propose that the tilting term is affected by convective momentum transport associated with precipitating systems crossing the boundary of the region, whereas the stretching term relies on the convergence and divergence induced by storms within the region. The simulation with parameterized convection captures the heating profile similarly to the simulation with explicit convection, but there are marked differences in convective momentum transport. An accurate vertical convergence structure as well as momentum transport must be simulated in parameterizations to correctly represent the impacts of convection on circulation.

SIGNIFICANCE STATEMENT: We used climate simulations with explicit convection and a convection parameterization to interrogate the relationship between mesoscale convection and synoptic-scale circulation over West Africa. We examined the typical behavior of mesoscale precipitating systems in both simulations and compared this with an observation of a storm. We also investigated how synoptic circulation changed over a diurnal cycle in both simulations. The biggest differences between the simulations were caused by how mesoscale systems in each simulation transport momentum when they cross the boundaries of a circulation, but the greatest impact on synoptic circulation was from the patterns of convergence and divergence induced by mesoscale systems, which are very similar in both simulations. Convection parameterizations should prioritize improving the representation of momentum transport.

KEYWORDS: Africa; Convective storms; Momentum; Vorticity; Cloud-resolving models; Convective parameterization

1. Introduction

Mesoscale convective systems (MCSs) are a defining feature of the West African climate during boreal summer. It is estimated that the most intense 12% of MCSs contribute about 90% of the precipitation in the region (Mathon et al. 2002), dominating overnight rainfall in particular (Vizy and Cook 2018). MCSs in West Africa are among the most intense on Earth (Zipser et al. 2006) and in recent years intense precipitation, especially from organized convection, is increasing (Panthou et al. 2012; Taylor et al. 2017; Panthou et al. 2018). Accurately representing MCSs is important because of their direct, significant impacts on local weather, and modulation of synoptic conditions (e.g., Parsons et al. 2019; Peters et al. 2019). However, MCSs can be difficult to predict because convective parameterizations struggle to accurately represent organized convection (Peters et al. 2019).

Understanding interactions between convective-scale diabatic processes and synoptic circulations is a major modeling challenge. Representation of clouds in the tropics is one of the largest sources of uncertainty in future projections of rainfall in climate models (Stevens and Bony 2013), and in West Africa there is no strong consensus on the modulation of precipitation under climate change (e.g., Rowell et al. 2016; Dosio et al. 2019). Simulating convection explicitly may provide insight into convective dynamics and their upscale effects, especially in the tropics where there are few detailed observations of convective systems.

West African weather is largely dominated by the West African monsoon (WAM), a seasonal reversal of surface winds over the region. This pattern, along with the temperature gradient between the Sahel and the Sahara, gives rise to the

Denotes content that is immediately available upon publication as open access.

Corresponding author: Fran Morris, eefamo@leeds.ac.uk; francesca.morris@ouce.ox.ac.uk

DOI: 10.1175/JAS-D-22-0032.1

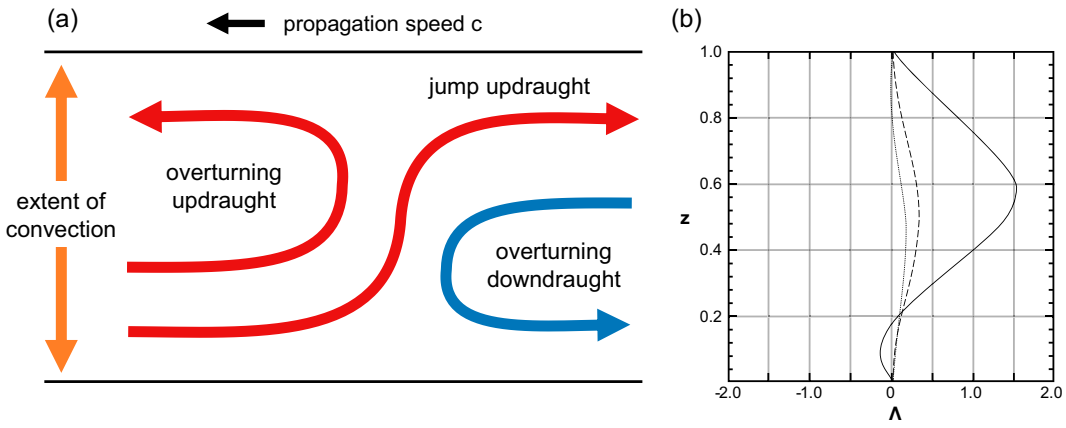

FIG. 1. Based on figures from Moncrieff (1992): (a) Schematic of "triple branch circulation" of storm-relative streamlines within a westward-propagating organized convective system. An overturning updraft at the front of the storm and a jump updraft flowing from the front to the rear of the storm are illustrated in red, and the downdrafts are in blue. (b) Normalized vertical profiles of momentum flux, $\Lambda = \langle \rho u_m w_m \rangle / \rho U_0^2$. The u_m and w_m are the storm-relative zonal and vertical velocities, ρ is the density of the inflowing air, and U_0 is the relative velocity of the inflow. The profiles are shown for triple branch circulation with an overturning updraft and overturning downdraft (dashed line), circulation without an overturning updraft (solid line), and circulation without an overturning downdraft (dotted line).

African easterly jet (AEJ), a midtropospheric zonal jet with a peak velocity at around 600–700 hPa and a latitude of around 13°–14°N in boreal summer (Fink et al. 2017). The AEJ is the source of African easterly waves (AEWs), westward-propagating synoptic-scale disturbances that travel along the AEJ between June and October. AEW formation is associated with barotropic-baroclinic instabilities in the AEJ (Eliassen 1983; Dickinson and Molinari 2000), and their initiation may also be linked to convection (Berry and Thorncroft 2005; Hsieh and Cook 2005; Mekonnen et al. 2006; Hsieh and Cook 2008; Thorncroft et al. 2008). Núñez Ocasio et al. (2020) and Russell et al. (2020) describe the collocation of convection with the front of an AEW trough, linked to moisture instability generated by the vertical heating of convection acting to strengthen AEWs. Núñez Ocasio et al. (2020) point out that convection associated with nondeveloping AEWs is usually located to the south of the trough. Currently, models for the interaction between convection and AEWs include the diabatic Rossby wave model (Parker and Thorpe 1995; Moore and Montgomery 2005) and the stratiform instability model (Mapes 2000; Kuang 2008; Russell et al. 2020). Tomassini (2018) suggests that MCSs tend to amplify existing AEWs by generating a potential vorticity (PV) signature ahead of the AEW trough, facilitating the AEW's maintenance, because a mature MCS will travel faster than an AEW.

Errors in AEW forecasts can be attributed to the limitations of convection schemes (Elless and Torn 2018). Regional convection-permitting models studies (e.g., the Cascade Project; Pearson et al. 2010) demonstrate the added value of representing convective dynamics explicitly, even on relatively coarse scales, in tropical West Africa (e.g., Marsham et al. 2013; Taylor et al. 2013; Birch et al. 2014b,a). Representation of convection has been shown to impact how models represent the WAM, which can have far-reaching impacts, even affecting forecasts in the North Atlantic–European sector (Pante and Knippertz 2019).

There are several efforts to better parameterize organized convection, especially in the tropics. Examples include the Khouider–Majda multicloud model (Khouider and Majda 2006), which characterizes heating structures of various convective modes, and the multiscale coherent structure parameterization (Moncrieff et al. 2017). Moncrieff's parameterization is based on theoretical momentum transport properties associated with propagating coherent cloud structures, discussed in detail in Moncrieff (1992). Archetypal systems are characterized by a triple-branch circulation of storm-relative winds, with a jump-like updraft flow through the system combined with an overturning updraft at the front of the storm and an overturning downdraft toward the rear (Fig. 1a). Assuming sheared background flow, heat and momentum transport can be deduced for an archetypal system and for other limiting regimes (e.g., with no overturning updraft, or no overturning downdraft; Fig. 1b). Idealized simulations have recreated the up- and downgradient momentum transport in such systems (Badlan et al. 2017).

In this paper, we use a convection-permitting regional configuration of the Met Office Unified Model (MetUM) to examine how precipitating storm systems impact synoptic-scale dynamics. Results are compared with representation of similar processes in a simulation with parameterized convection. Synoptic circulation is quantified by examining the diurnal cycle of circulation tendency and the circulation budget terms associated with changes in circulation, outlined in section 3. In section 4 we characterize the properties of mesoscale convection in both simulations by compositing around precipitating features, demonstrating how dynamics around a statistically typical mesoscale precipitating system link to the circulation budget terms and discussing them in the framework of the Moncrieff model of momentum transport. The simulated dynamics are also compared with an observational case study using dropsonde observations of an MCS from the JET2000 project (Thorncroft et al. 2003). Conclusions are given in section 5.

2. Data

This study compares two regional climate configurations of the MetUM: CP4-Africa (CP4), a convection-permitting simulation with a resolution of 4.4 km at the equator, and a similar regional simulation with parameterized convection and a resolution of 25 km at the equator (R25). The simulations are 10-yr free-running "current climate" simulations with lateral boundary conditions supplied by a 25-km-grid-spacing GCM configured similarly to R25. R25 uses the 6A convection scheme as in the Global Atmosphere 7.0 MetUM setup (Walters et al. 2019) and the prognostic cloud fraction and prognostic condensate (PC2) scheme (Wilson et al. 2008). CP4 directly simulates deep convection and uses the Smith (1990) diagnostic large-sale cloud scheme and Wilson and Ballard (1999) microphysics scheme. CP4 uses a blended boundary layer scheme (Boutle et al. 2014) that combines the schemes of Lock et al. (2000) and Smagorinsky (1963), which are better suited to low- and high-resolution models, respectively, whereas R25 does not require a blended scheme. Full details of the model setup may be found in Stratton et al. (2018).

a. CP4 and R25 evaluation

With a 4.4-km grid, CP4 cannot explicitly represent dynamics of shallow convection or congestus clouds, but it does improve diurnal precipitation timing and intensity relative to the 6A convection scheme used in R25 (Stratton et al. 2018; Kendon et al. 2019), especially when rainfall is regridded to 25-km resolution (Berthou et al. 2019). CP4 also improves representation of the WAM and frequency of MCSs in relation to observations (Stratton et al. 2018; Berthou et al. 2019). The CP4 MCSs have more realistic lifetimes, spatial distributions, and propagation directions than those of R25 but are smaller and propagate slower than observed systems (Crook et al. 2019). Fitzpatrick et al. (2020) note that the response of the MCSs to shear is not as expected, with no correlation between shear and precipitation despite observational and idealized model evidence that shear facilitates MCS organization (e.g., Rotunno et al. 1988; Alfaro 2017; Bickle et al. 2021; Klein et al. 2021; Baidu et al. 2022).

b. Region and time domain selection

Our analysis uses 3-hourly pressure-level wind, temperature, and moisture fields, and hourly precipitation data, during July and August (season of peak WAM activity) in the current-climate simulations. CP4 data were regridded to R25's resolution to minimize the impact of their different resolutions.

The region chosen was a box that has its southwestern corner at 7.5°N, 10°W and its northeastern corner at 15°N, 5°E, as illustrated in Fig. 2. The region was selected so that it was located entirely over land, not covering any major orographic features, and so that the box largely covers the zonal wind speed maximum of the AEJ. The box covers the southern AEW track (Pytharoulis and Thorncroft 1999; Fink et al. 2017), which is strongly associated with Sahelian moist convection. A fixed region was analyzed because the AEJ is geographically constrained by the moisture gradient between the Sahel and the Sahara (Schubert et al. 1991; Thorncroft and Blackburn 1999; Wu et al. 2009).

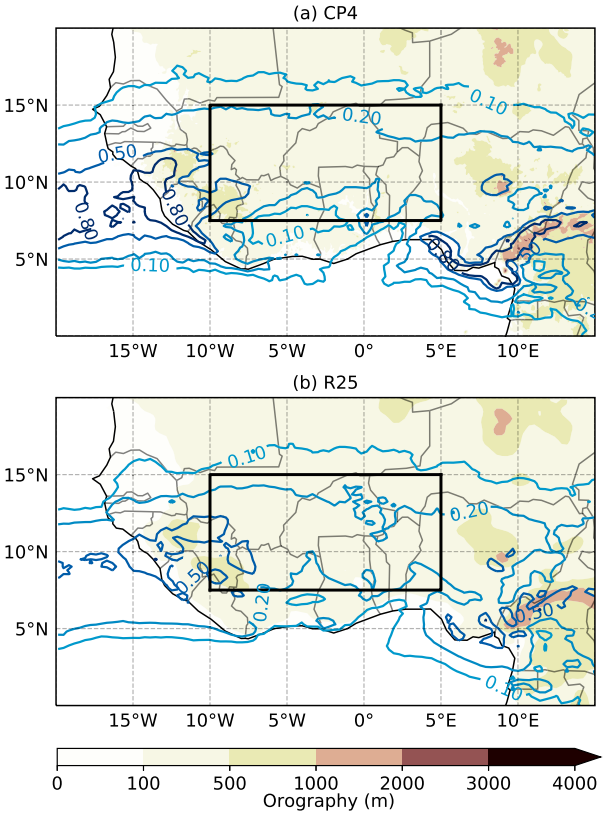

FIG. 2. Orography (filled contours; m) and mean rainfall (line contours, labeled in millimeters per hour) in July and August 1998–2006 for (a) CP4 and (b) R25. The region of interest analyzed in this paper is outlined by the black box.

We analyzed dynamics relative to the diurnal cycle because free-running climate simulations will diverge significantly within the domain, so individual weather events in different simulations will not directly correspond to each other and therefore cannot be compared on a case-by-case basis. Furthermore, the processes that dominate West African weather systems are fundamentally diurnal in nature (Parker et al. 2005b), especially over land. With a diurnal framework we can separate processes according to time of day and understand the causes and impacts of diurnal activity. The precipitating convection that we analyze is divided into two regimes within the diurnal cycle: "afternoon" convection (1200–1800 UTC) and "overnight" convection (2100–0300 UTC). Convection in the afternoon tends to be less organized than overnight convection, which usually consists of mature MCSs (Vizy and Cook 2018).

c. Observational data

Measurements from the JET2000 observational campaign (Thorncroft et al. 2003; Parker et al. 2005a) of a storm in August of 2000 were used. We examine the dropsondes launched from flight A781, which flew within the mesoscale circulation behind (to the east of) a decaying storm at around 1100 UTC 29 August 2000. Thorncroft et al. (2003) give further details (flight 3 listed in their Table 1). The east leg of

flight A781 is along a constant longitude of approximately 2.2°E from 8° to 18°N before turning around and passing behind the storm located at roughly 11°N.

3. Circulation and the circulation budget

The framework we use in this paper to separate physical processes on the synoptic scale is through a circulation budget. In this section, we discuss the strengths of this framework, calculate it for the selected region, and explain how different terms are related to the diurnal processes associated with the WAM.

Circulation Γ is the contour integral of velocity $\mathbf{u}$ around some closed contour C, equivalent to the surface integral of vorticity η contained in a region S enclosed by C. Circulation, therefore, is a large-scale quantity encapsulating smaller-scale dynamics within a region, making it a powerful tool for examining scale interactions. By formulating a circulation budget, and analyzing the magnitude of different terms, we can also interrogate physical processes.

The equation for absolute vorticity η (sum of relative vorticity ζ and planetary vorticity f), can be written in flux form:

$$\frac{\partial \eta}{\partial t} = -\nabla_{xy} \cdot \mathbf{J}, \quad \text{where}$$

$$\mathbf{J} = \begin{pmatrix} u\eta + \omega\dfrac{\partial v}{\partial p} - G \\ v\eta - \omega\dfrac{\partial u}{\partial p} + F \end{pmatrix} = \mathbf{u}\eta - \omega\hat{\mathbf{k}} \times \frac{\partial \mathbf{u}}{\partial p} + \hat{\mathbf{k}} \times \mathbf{F}. \qquad (1)$$

Here, ∇_{xy} is the differential operator in the x and y directions, $\mathbf{F} = (F, G)$ is frictional forces, and $\hat{\mathbf{k}}$ is the unit vector along the p axis. Terms represent the accumulation of vorticity horizontally through the sides of the box on consistent pressure surfaces ($\mathbf{u}\eta$), the vertical tilting of horizontal vorticity into the vertical vorticity component $[-\omega\hat{\mathbf{k}} \times (\partial\mathbf{u}/\partial p)]$, and frictional terms ($\hat{\mathbf{k}} \times \mathbf{F}$). Haynes and McIntyre (1987) suggest splitting the velocity and vorticity elements into mean and perturbation elements for greater insight into processes at different scales.

We let $\mathbf{u} = \overline{\mathbf{u}} + \mathbf{u}'$, $\eta = \overline{\eta} + \eta'$, and $\omega = \overline{\omega} + \omega'$, where the bars denote our choice of mean, taken at each grid cell over each hour in the diurnal cycle, and dashed quantities are perturbations from this mean. Taking the same mean over the entire equation and integrating over a closed pressure surface S enclosed by contour C:

$$\frac{\partial \overline{\Gamma}}{\partial t} = -\iint_S \nabla_{xy} \cdot \left(\overline{\mathbf{u}}\,\overline{\eta} + \mathbf{u}'\eta' - \overline{\omega}\hat{\mathbf{k}} \times \frac{\partial \overline{\mathbf{u}}}{\partial p} - \omega'\hat{\mathbf{k}} \times \frac{\partial \mathbf{u}'}{\partial p} + \hat{\mathbf{k}} \times \mathbf{F} \right) dS \qquad (2)$$

$$\frac{\partial \overline{\Gamma}}{\partial t} = -\oint_C \Bigg(\underbrace{\overline{\mathbf{u}}\,\overline{\eta}}_{\text{synoptic accumulation}} + \underbrace{\mathbf{u}'\eta'}_{\text{anomalous accumulation}} \underbrace{-\overline{\omega}\hat{\mathbf{k}} \times \frac{\partial \overline{\mathbf{u}}}{\partial p}}_{\text{synoptic tilting}} \underbrace{-\omega'\hat{\mathbf{k}} \times \frac{\partial \mathbf{u}'}{\partial p}}_{\text{synoptic tilting}} + \underbrace{\hat{\mathbf{k}} \times \mathbf{F}}_{\text{friction}} \Bigg) \cdot \hat{\mathbf{n}}\, dl. \qquad (3)$$

This equation is the circulation budget. The five terms in this equation allow us to characterize how different processes at different scales govern changes to synoptic-scale circulation, over the diurnal cycle. Similar techniques have been used to analyze the circulation budgets associated with tropical cyclones (e.g., Raymond and Sessions 2014).

Figure 3 shows the mean diurnal circulation and circulation tendency around the box illustrated in Fig. 2. There are distinct diurnal patterns in circulation in both simulations, with the strongest variation at 1000–850 hPa, but there are several differences between the two simulations. At 400–500 hPa, circulation is stronger and more strongly varying in CP4 than in R25. Generally, however, the circulation tendency in R25 has a greater magnitude, especially at around 800 hPa. Also, the patterns in CP4 lag those in R25 by around 3 h. The lag corresponds with the difference in peak rainfall time shown by the solid black line in Fig. 3, which is at 1500 UTC in CP4 and 1200 UTC in R25 (Stratton et al. 2018; Berthou et al. 2019). To understand what processes cause the differences in circulation and circulation tendency, we calculate the circulation budget terms described by Eq. (3) over a diurnal cycle (Fig. 4).

Anomalous and synoptic terms theoretically split the budget into contributions from diurnal synoptic motions and effects from individual storms. However, this division is not precise since convection is a strongly diurnal process itself, and intrinsically linked to the synoptic diurnal weather systems such as the WAM. Therefore, some effects of convection on the circulation budget will be contained within the synoptic circulation budget terms rather than the anomalous terms.

We explain the patterns in the synoptic terms in Figs. 4a, 4b and 4e, 4f in the context of the WAM. First, note that the background absolute vorticity of the region is general positive due to planetary vorticity f. In the morning, over land in West Africa, solar radiation causes surface heating, leading to ascent in dry convection in the north of the region over the Sahara from low to midlevels, associated with the negative tendency in the synoptic tilting term that peaks at 0900 UTC in R25 and a little later in CP4 (Figs. 4e,f). Turbulent mixing associated with convection disrupts the southerly monsoon flow that has developed overnight (see Parker et al. 2005b), especially in the north, causing convergence within the box. Given the positive background vorticity, this leads to low- to midlevel synoptic-scale accumulation as convection begins in both simulations. CP4 (Fig. 4a) has smaller and later synoptic accumulation than R25 during hours of afternoon convection because of the delay in the daily onset of convection, and because CP4's monsoon flow extends farther north (Jackson et al. 2022), so there is less synoptic convergence in the box. It is for the same reason that CP4's tilting tendency is weaker than R25: the ascent over the Sahara is farther north and the northern edge of the box behaves more similarly to its southern edge than in R25. Jackson et al. (2022) also note that CP4's ascent tends to be deeper and more intense, which may account for the greater vertical extent of CP4's circulation tendencies.

Above the monsoon flow, there is a northerly return flow at midlevels. Since the northern edge of the monsoon flow has been disrupted, this now only exists in the southern edge of the box, causing an overall divergence signature at 600 hPa as convection

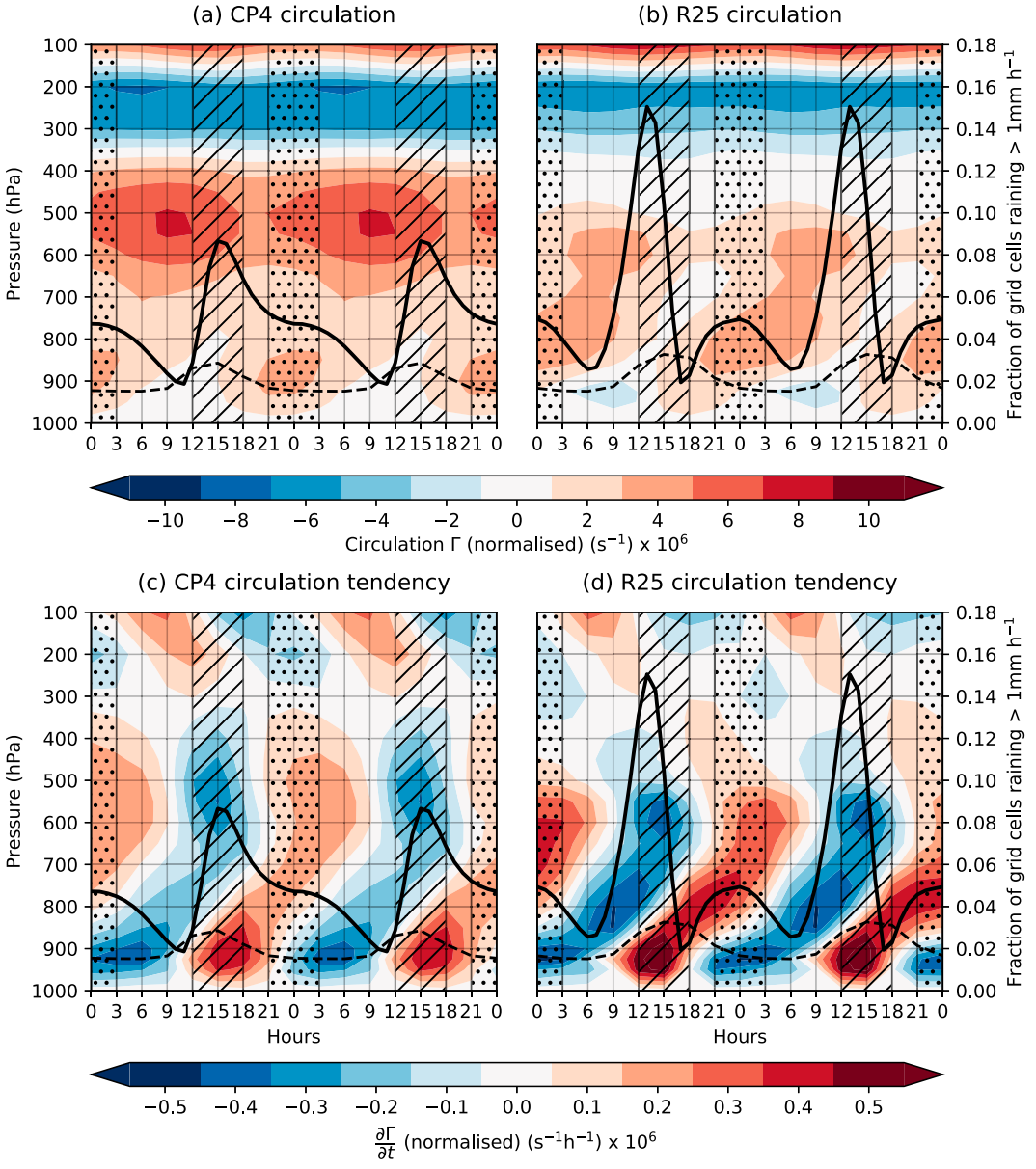

FIG. 3. Mean diurnal cycle (repeated for two full days) of (a),(b) normalized circulation Γ (filled contours) and (c),(d) normalized circulation tendency $\partial\Gamma/\partial t$ (filled contours) around the synoptic region illustrated in Fig. 2, for (left) CP4 and (right) R25. Also shown is rainfall fraction [fraction of grid cells with a precipitation rate of 1 mm h^{-1} or greater (black solid line)] and estimated convective boundary layer height (dashed black line). The diagram also indicates the regions selected for "afternoon" (1200–1800 UTC; hatched) and "overnight" (2100–0300 UTC; stippled) convection.

initiates, in both simulations, associated with the negative synoptic accumulation anomaly. By contrast, the synoptic accumulation at 200 hPa remains negative for almost the entire diurnal cycle in both simulations. This level is dominated by the behavior of the tropical easterly jet, which peaks at 8°N near the southern edge of the box. In CP4, there is lower positive absolute vorticity during the hours of active convection, perhaps due to the deeper convection in CP4 and associated upper-level negative vorticity anomalies (see section 4a), reducing the negative anomaly in synoptic accumulation relative to R25 in the early afternoon.

Overnight, diurnal convection dies down, beginning with the north of the region and leading to subsidence on the northern edge of the box, while significant convection remains active to the south of the box. The meridional variance in ascent is associated with the positive tilting term anomalies in the early evening at 850 hPa. Around 0000–0300 UTC, the convection on the southern edge also begins to wane, leading to southern subsidence that reverses this tilt and results in the negative tilting term in the early hours of the morning.

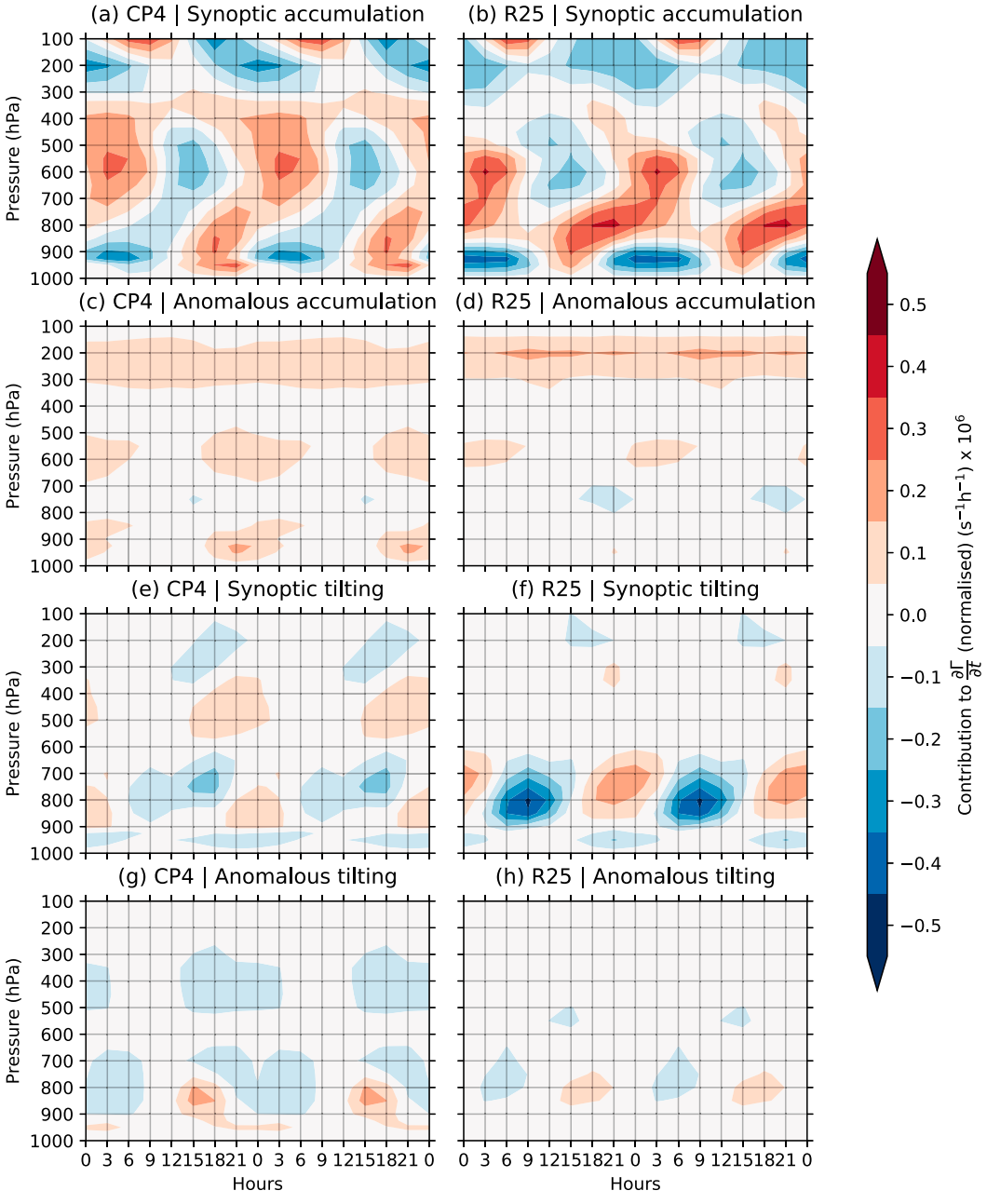

FIG. 4. Mean diurnal cycle (repeated for two full days) of circulation budget terms: (a),(b) "synoptic accumulation" term $-\oint_C \overline{\mathbf{u}}\,\overline{\boldsymbol{\eta}} \cdot \hat{\mathbf{n}}\, dl$; (c),(d) "anomalous accumulation" $-\oint_C \mathbf{u}'\boldsymbol{\eta}' \cdot \hat{\mathbf{n}}\, dl$; (e),(f) "synoptic tilting" $-\oint_C \overline{\omega}\hat{\mathbf{k}} \times (\partial\overline{\mathbf{u}}/\partial p) \cdot \hat{\mathbf{n}}\, dl$; and (g),(h) "anomalous tilting" $-\oint_C \omega'\hat{\mathbf{k}} \times (\partial\mathbf{u}'/\partial p) \cdot \hat{\mathbf{n}}\, dl$.

As convection diminishes, surface monsoon flow resumes and reaches its full extent beyond the north of the box. The flow advects positive planetary vorticity northward, replacing vorticity in the region with lower-magnitude vorticity and resulting in a low-level negative accumulation term overnight from 0000 to 0900 UTC. The anomaly is larger in R25 than CP4 because the monsoon flow in R25 is stronger (Jackson et al. 2022). Again, there is a northerly return flow at midlevels with the opposite effect at the same time, causing positive accumulation from 800 to 600 hPa (up to 400 hPa in CP4).

A major unanswered question that remains from our process-based analysis is the cause of the extended vertical signature in the tilting term during the afternoon in CP4. Contributions of convection to the synoptic and anomalous terms will be examined in more detail as we explore mesoscale dynamics in the model in section 4.

We were unable to estimate the frictional term adequately from the data available. We calculated the residual between the total circulation tendency and the known terms (not shown), which would include the effects of friction. We would

expect friction to have maximum intensity at low levels in the convective boundary layer (CBL) during peak hours of convection. As a proxy we estimate the CBL height (dashed black line in Fig. 3) using profiles of virtual potential temperature θ_v averaged through the region, defining CBL height as the first vertical pressure level where θ_v has decreased by 1 K from its value at 950 hPa. The estimated residual does peak in the expected periods of high turbulence, but is significant even at upper levels, where it cannot be attributed to friction. The discrepancy is caused by the low (3-h) time resolution, leading to noninstantaneous and imprecise derivatives.

CBL height peaks during the hours of active afternoon convection and drops to a minimum in the early hours of the morning. R25's afternoon boundary layer is slightly deeper than CP4's, and in it there is a strong positive circulation tendency anomaly that is delayed and less intense in CP4, perhaps due to CP4's blended boundary layer scheme (see section 2). Since this positive anomaly is not accounted for in the other terms in the circulation budget (Fig. 4), it is likely to be a result of the friction term.

4. Dynamics of mesoscale precipitating features

To investigate whether the contributions to the circulation budget may be attributed to MCSs, in this section we characterize the dynamics of precipitating features on the mesoscale.

We composite features of 500-km boxes centered on grid cells precipitating at a rate greater than 1 mm h^{-1} (considered the threshold for rainfall to significantly affect soil moisture). The composites are taken for all grid cells precipitating above these thresholds during the afternoon (1200–1800 UTC) and overnight (2100–0300 UTC). During the selected period, in CP4 127 443 precipitating grid cells were identified during the afternoon regime and 100 324 overnight. R25 had 178 839 and 95 158 precipitating grid cells in the afternoon and overnight regimes, respectively (consistent with the fraction of precipitating grid cells in Fig. 3).

In the following sections, we link the composites to processes that control synoptic circulation by plotting the dynamical features that relate to the accumulation ($-\oint_C \mathbf{u}\eta \cdot \hat{\mathbf{n}}\, dl$) and tilting [$-\oint_C \omega\hat{\mathbf{k}} \times (\partial\mathbf{u}/\partial p) \cdot \hat{\mathbf{n}}\, dl$] terms in the circulation budget.

a. *Accumulation by precipitating features on the mesoscale*

Since accumulation is the flux of vorticity into the region, the anomalies (relative to the mean at a given point at a given time in the diurnal cycle) of absolute vorticity and divergence associated with precipitating grid cells were composited (Fig. 5). Meridional (north–south) composites in both CP4 and R25 show meridional dipoles of relative vorticity, with low-level convergence and upper-level divergence implying the existence of an updraft between the two. Overnight, composites show midlevel convergence up to around 450 hPa (Figs. 5c,d). Composites around grid cells with rainfall under 1 mm h^{-1} have negligible vorticity and divergence signatures (not shown), suggesting that the convective dynamics in Fig. 5 are robustly associated with precipitation.

CP4 has a narrower, more intense vorticity dipole than R25 with a greater vertical extent, from about 850 hPa to over 200 hPa in the afternoon. In R25, the dipole exists at around 800–700 hPa in the afternoon and is around 5 times weaker. The dipole is consistent with lifting of vortex tubes (caused by the climatological vertical background shear) by vertical velocity associated with convection (e.g., Holton 2004), and most simulations of squall lines in West Africa (Rotunno et al. 1988), although case studies of some examples have a reversed north–south orientation (Diongue et al. 2002). The positive anomalies are more pronounced and extensive than the negative, due to the positive background planetary and relative vorticity (induced to the south of the AEJ due to the AEJ's zonal shear profile) being intensified by vortex stretching.

Both simulations have low-level convergence (negative divergence field) and upper-level divergence within around 150 km of the central precipitating point in the afternoon convection and expanding to around 200 km overnight. The convergence in CP4 is more sustained toward midlevels relative to R25. In both simulations, the vorticity and divergence signatures intensify overnight, where typically a larger fraction of convection is organized, and in CP4 the signatures widen and are elevated, indicating a significant structure modulation. Storms in R25 do not travel in such a uniform direction as those in CP4, which may impact the vorticity intensity, alongside the parameterization being associated with a weaker updraft. The parameterization may also not be reliably representing midlevel convection during the afternoon hours.

The product of vorticity and divergence approximately corresponds to the accumulation term's integrand. It is negative for almost the entire column, with intensity peaking at around 900 and 200 hPa. Therefore, particularly at lower and upper levels, precipitating systems contribute positively to the circulation budget through accumulation [see Eq. (3)] associated with storm-induced convergence pulling positive absolute vorticity into the region, increasing circulation. The same process may occur at midlevels where there is elevated convection. At upper levels, storm-induced divergence pushes negative vorticity anomalies associated with storms out of the box, which similarly contributes positively to the circulation tendency. The process of mesoscale convection therefore reinforces cyclonic circulation on the synoptic scale at lower and upper levels as reflected in Figs. 4g and 4h, and at midlevels in CP4, implying there is more elevated convection. The more intense positive low-level anomalous accumulation in CP4 can be explained by the stronger vorticity and divergence signatures than R25.

As discussed in section 3, the effects of precipitating convection may still be reflected in the synoptic accumulation term. For example, the height of the vorticity dipoles in CP4's composites can explain why the vertical signature of synoptic accumulation is more elongated in CP4 than R25, and the stronger negative vorticity anomalies at upper levels reduce the overall positive absolute vorticity and thus decrease the negative synoptic accumulation tendency at 200 hPa when convection is active.

b. *Tilting by precipitating features on the mesoscale*

To understand how mesoscale precipitating features modulate the tilting term, we composite its integrand of the tilting term, [$\omega\hat{\mathbf{k}} \times (\partial\mathbf{u}/\partial p)$] along 500-km cross sections centered on grid cells precipitating at a rate greater than 1 mm h^{-1}. The direct contributions to the circulation budget are from the

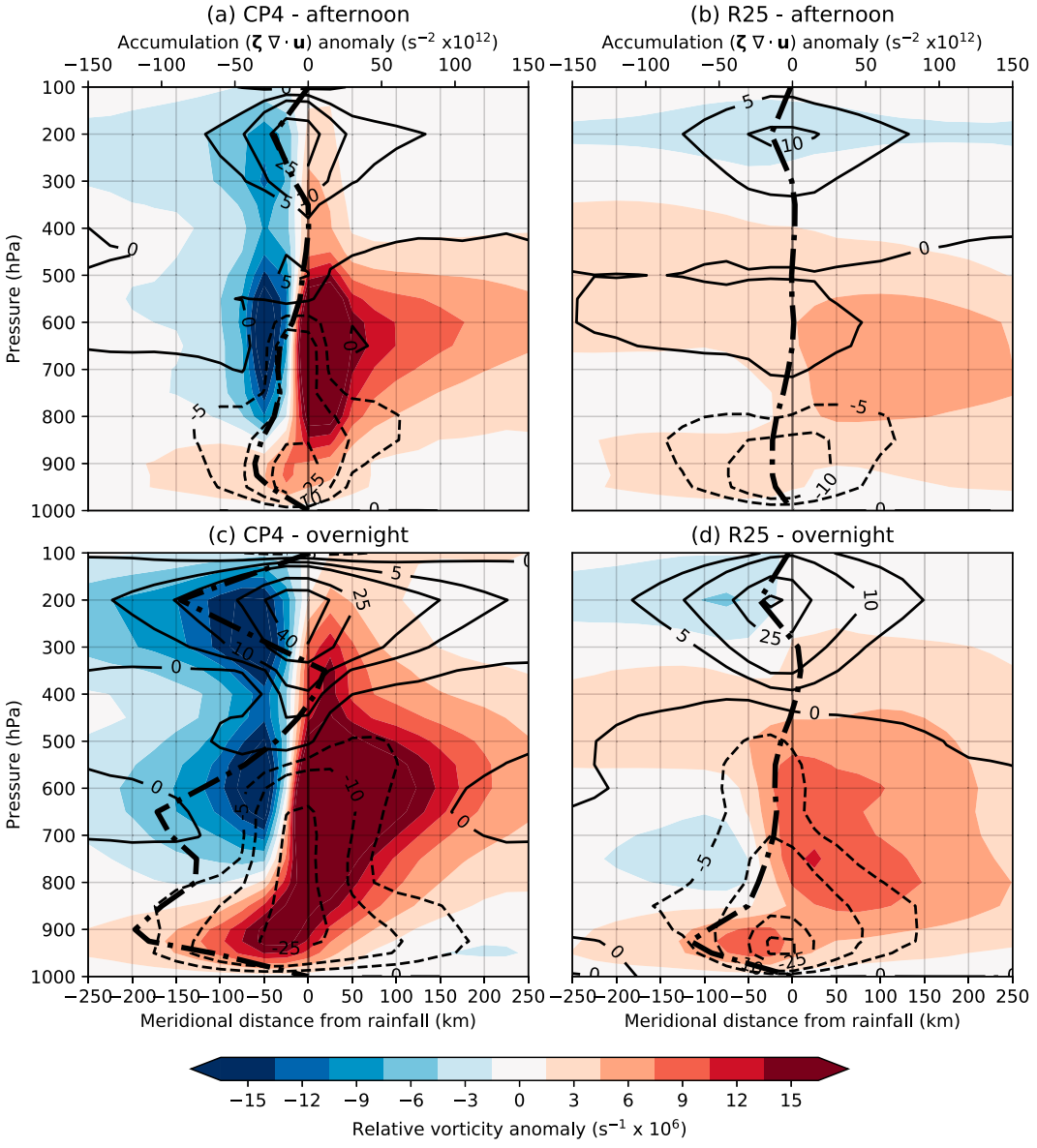

FIG. 5. Composites of relative vorticity anomaly (filled contours) and divergence anomaly (line contours) across a meridional (north–south) cross section of 500 km around grid cells precipitating at a rate of 1 mm h^{-1} or greater. Divergence anomaly is labeled in inverse seconds times 10^6; dashed lines represent negative values (convergence). The thick black dot–dashed line shows the product of the divergence and vorticity anomalies, averaged meridionally across the composite.

components of $\omega(\partial \mathbf{u}/\partial p)$ facing outward along each side of the box. For the northern and southern edges, the integrands are $\omega(\partial u/\partial p)$ and $-\omega(\partial u/\partial p)$, respectively, and, for the east and west borders, they are $-\omega(\partial v/\partial p)$ and $\omega(\partial v/\partial p)$, respectively. In this section, we examine both meridional (north–south) composites of $\omega(\partial v/\partial p)$ and zonal (east–west) composites of $\omega(\partial u/\partial p)$.

The net contribution of precipitating systems to the tilting term over the whole synoptic region is proportional to the difference between the number of precipitating pixels on the north and south or east and west box edges, and the corresponding integrand term. The number of precipitating grid cells on each edge of the box for the afternoon and overnight phases of convection are shown in Table 1 and are consistent, during the afternoon, with the climatological rainfall distribution (Fig. 2). There is a greater difference in precipitating grid cells between the eastern and western (meridional) edges than the difference between the northern and southern (zonal) edges, so the tilting term integrand along the west edge should contribute most strongly to the circulation budget.

In CP4, the meridional composites of $\omega(\partial v/\partial p)$ show a tripole, with a negative anomaly up to around 700 hPa, which then

TABLE 1. Number of grid cells precipitating at a rate of 1 mm h^{-1} or greater along each edge of the synoptic box for the two regimes of convection.

	South border	East border	North border	West border
	No. of precipitating cells in CP4 along each border			
Afternoon (1200–1800 UTC)	3004	2545	3499	3831
Overnight (2100–0300 UTC)	1886	2097	2306	4715
	No. of precipitating cells in R25 along each border			
Afternoon (1200–1800 UTC)	5515	4038	4614	5479
Overnight (2100–0300 UTC)	3124	1702	872	5726

becomes a positive anomaly until around 400 hPa and negative again up to 300 hPa (Fig. 6). R25 similarly has a low-level negative anomaly with a midlevel positive anomaly but has a greater meridional extent. The overnight convection composites (Figs. 6c,d) look more similar between the two models, with stronger low-level negative anomalies and positive anomalies extended from around 650 hPa to upper levels.

The zonal composites of $\omega(\partial u/\partial p)$ (Fig. 7) have anomalies that are up to around 5 times as intense as the meridional

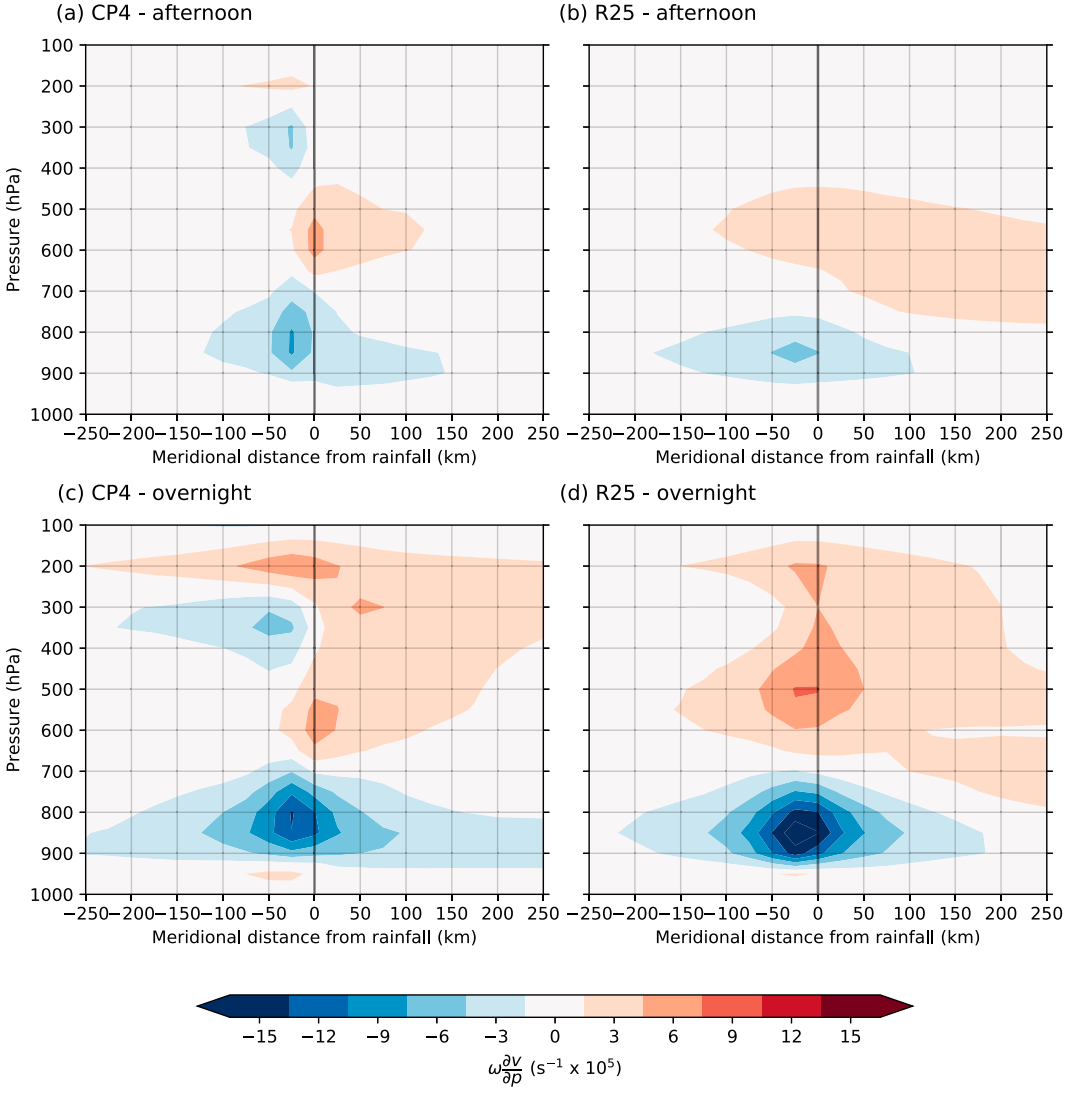

FIG. 6. Composites of tilting term integrand $[\omega(\partial v/\partial p)]$ anomaly across a meridional (north–south) cross section of 500 km centered on grid cells precipitating at a rate of 1 mm h^{-1} or greater. This contributes to the tilting integral through the eastern and western edges of the box.

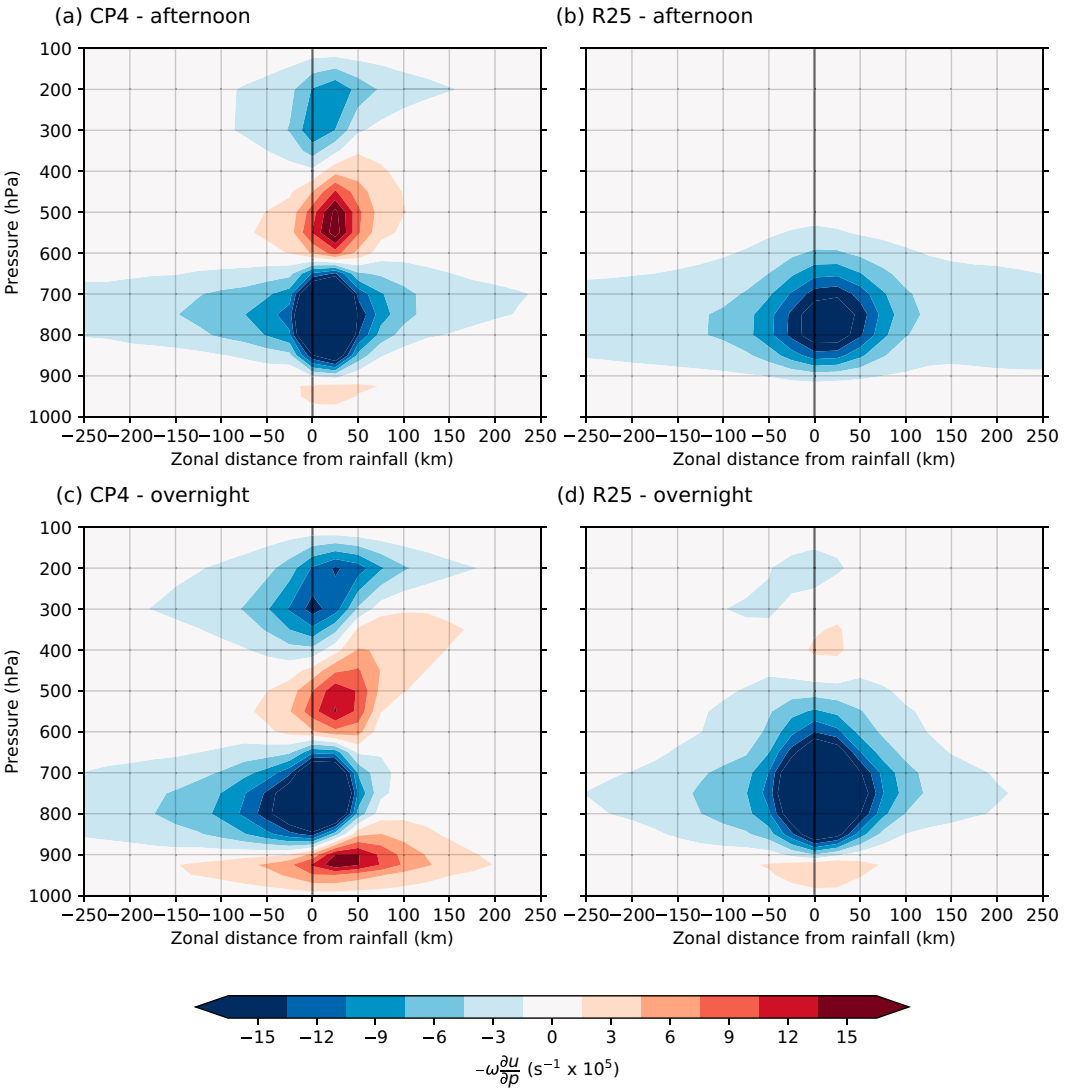

FIG. 7. Composites of tilting term integrand $-[\omega(\partial u/\partial p)]$ anomaly across a zonal (east–west) cross section of 500 km centered on grid cells precipitating at a rate of 1 mm h^{-1} or greater. This contributes to the tilting integral through the northern and southern edges of the box.

composites (Fig. 6) in afternoon convection, and almost twice as intense in overnight convection. While there is a greater difference in the number of precipitating grid cells between the eastern and western borders, the differences between the northern and southern borders may contribute just as strongly as the meridional composites to the total tilting term due to their greater intensity. Since there is more rainfall along the northern (southern) edge in CP4 (R25), the zonal composite signatures would contribute positively (negatively) to the total tilting term in the circulation budget. Note the difference in rainfall distribution in the two simulations, attributable to the more northern position of the WAM system in CP4 (Jackson et al. 2022). The zonal composites' tripole signature is very localized to the center of the precipitation. R25's signature is limited to a negative anomaly at 900–500 hPa, slightly more intense and extended in the overnight composite than the afternoon.

The structures in the tilting integrand composites are somewhat reflected in the CP4 synoptic tilting term (Fig. 4e), where the tripole structure appears during the hours of active afternoon convection. Both the western (Fig. 6) and northern (Fig. 7) edge contribute a negative anomaly at low levels, a positive anomaly at midlevels, and a negative anomaly at upper levels to the tilting integrand. This is superimposed over the synoptic tilting associated with monsoon ascent and subsidence discussed in section 3. R25 does not have any sign of tripole signatures in the synoptic term. Again, the effect of these MCSs is not necessarily a synoptic process: when anomalies around nonprecipitating grid cells are plotted (not shown) there is no signal at all, so the anomalies in the tilting integrand composites are robustly associated with precipitation. The diurnal convection is simply projected onto the synoptic tilting term. The signature of the anomalous tilting term, while small in

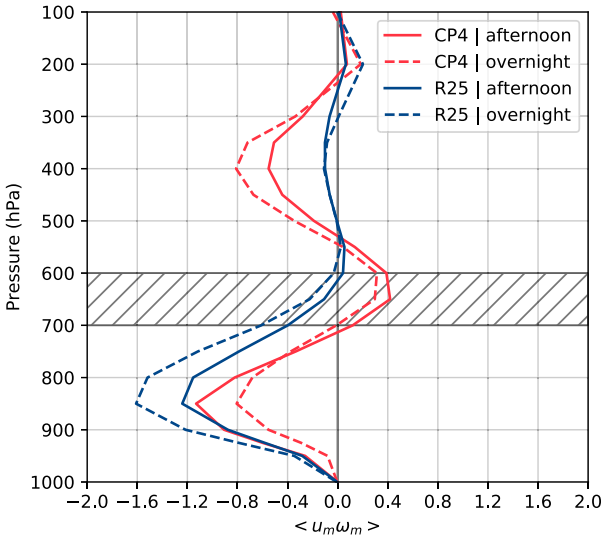

FIG. 8. Vertical profiles of the mean product of composited storm-relative zonal velocity u_m and vertical velocity ω_m for CP4 (red lines) and R25 (blue lines) through afternoon convection 1200–1800 UTC (solid lines) and overnight convection 2100–0300 UTC (dashed lines). The mean values are calculated at each pressure level for the entire width of the zonal composites in Fig. 7. The hatched region represents the typical height of the AEJ.

magnitude, tends to oppose the sign of the synoptic tilting term; this is likely as a result of storms on the opposite sides of the box to where rain dominates.

We now examine the convective momentum transport of a typical precipitating system, since the tilting integrand is connected in some respects to the convective momentum transport, $\langle \rho u_m \omega_m \rangle$, defined in section 1. This relationship is explored in more detail in the appendix. Following Moncrieff (1992), we estimate convective momentum transport profiles across precipitating systems. Storm-relative winds are calculated by subtracting the mean of the zonal velocity u across all points in the composite from 700 hPa and above from individual points in the composite. These propagating speeds are not likely to be accurate for individual systems, but they were of appropriate magnitude. The vertical profile is estimated by taking a mean of $u_m\omega_m$ across each pressure level in a 500-km zonal length centered on the precipitating grid cell. In Moncrieff (1992), the mean is taken over every point where the system has modulated the background wind field and normalized, whereas we take the mean across a set length (for simplicity, since the size of a storm and its influence over the local wind profile is highly variable) and we have not normalized the values using inflow velocity.

Figure 8 shows the vertical profile of convective momentum transport for CP4 and R25. We would expect the reversal of the Fig. 1b signature since we use pressure rather than height coordinates, but we observe two negative momentum peaks instead of one, at around 850 and 400 hPa. The upper peak is more intense in the CP4 profile. In the zonal velocity anomaly field (not shown) we see a double overturning updraft to the west of the system center in CP4 rather than a single overturning updraft in the archetypal triple-branch circulation (Fig. 1a). Each momentum transport peak is associated with one of those updrafts, and the positive peak at around 600 hPa in CP4 is associated with a third overturning updraft to the east of the storm. The lower-level peak in overnight CP4 is less intense than the corresponding afternoon peak, which could be due to a downdraft in the zonal wind field dampening the momentum transport signature (Fig. 1b).

R25 only has one peak and one overturning updraft. Overnight, R25's lower-level momentum transport increases while CP4's decreases. R25's change between afternoon and overnight convection appears to be an intensification of the same structure, while CP4 seems to be adjusting its structure to represent more elevated convection, suggesting that CP4 represents organized systems with dynamics that change depending on their maturity and time of day. The pressure derivative of the convective momentum transport pattern (Fig. 7) is similar to the pressure derivative of the patterns shown by the convective momentum transport estimated in Fig. 8. Therefore, it is likely that the representation of convective momentum transport in storms leads to impacts on the circulation budget through the tilting term.

The direct impacts of convective momentum transport on the tilting term are on the edges of the box; there are also indirect impacts. By modulating the wind field around the storm, the momentum transport may lead to changes in the vorticity accumulation patterns on the mesoscale and upscale. Of course, if a perfect vorticity dipole is contained within the circulation then it will have no net impact on the circulation, but, as shown in Fig. 5, dipoles associated with convection are rarely symmetrical, so the vorticity accumulation may be modulated as vortex stretching enhances dipole asymmetry. Also, the momentum transport could modulate the overall zonal wind field within the box, impacting the synoptic winds beyond that which can be measured by circulation. Understanding these effects would require significant momentum budget analysis, which we felt was beyond the scope of this paper.

c. *Comparison with observations*

We compare the composited precipitation features with an observed storm from August of 2000, with measurements taken by dropsondes from a plane flying through a decaying storm at around 1100 UTC. Since the plane flew along a single latitude the measurements are not instantaneous nor can they provide a complete calculation of vorticity, but we estimate the component of vertical vorticity from the variation of zonal velocity along latitude $[-(\partial u/\partial y)]$ as the plane flew by (Fig. 9a). There is a dipole structure present just below 600 hPa. The horizontal resolution is limited by the distance between sondes dropped (0.5°, or around 55 km), so the precise scale of the dipole is unclear, but it is almost certainly constrained within 100 km either side of its center. Below 800 hPa, a reversed dipole structure signature exists, forming a quadrupole that extends to around 200 km on either side of the storm's center. Figure 9 also shows the $\partial v/\partial y$ component of divergence. There is a divergence signature from around 900 to 750 hPa within around 100 km of the storm, with smaller regions of convergence

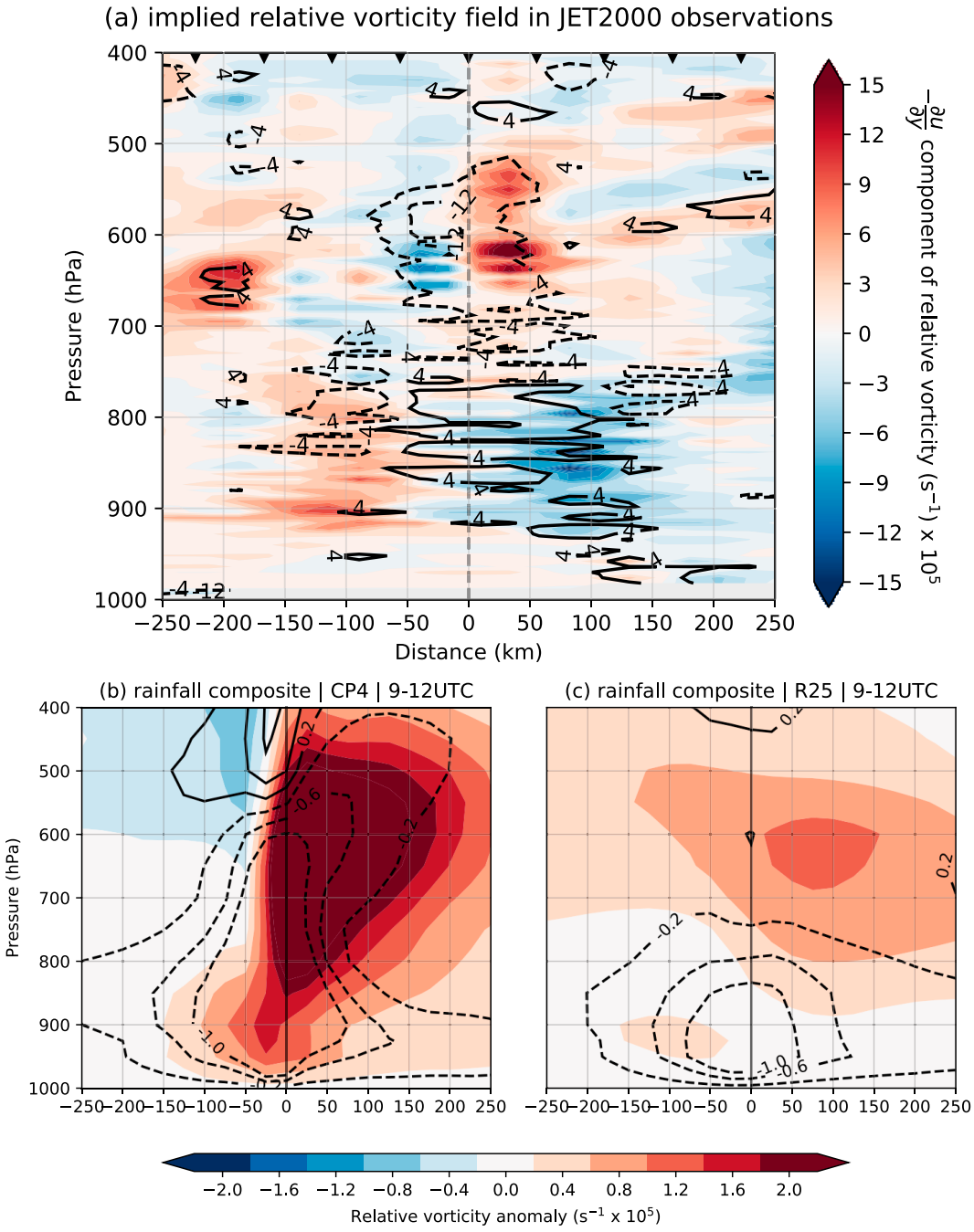

FIG. 9. (a) Meridional cross section of the relative vorticity term contributed by latitudinal change in zonal velocity, $-(\partial u/\partial y)$ (shading), and the horizontal divergence from meridional velocity variation, $\partial v/\partial y$ (line contours, labeled in inverse seconds times 10^6), spanning 500 km centered on the storm at 11°N (black dashed line). Also shown are meridional cross sections of relative vorticity and divergence anomaly in composites around grid cells precipitating at a rate greater than 1 mm h^{-1} in (b) CP4 and (c) R25 at 0900–1200 UTC over the same pressure range as (a).

100–200 km from the center of the storm between 850 and 750 hPa. Above 700 hPa, there is convergence at the center of the vorticity dipole up to 500 hPa.

Figures 9b and 9c, plotted following Fig. 5, are composites of relative vorticity and divergence anomalies around precipitating grid cells in CP4 and R25, respectively, over the same height range as the observations in Fig. 9a, taken over all July and August days for 0900–1200 UTC to approximately match the observation time on this flight. (In CP4, 36 630 grid cells are included in the period, and in R25 there are 126 772.)

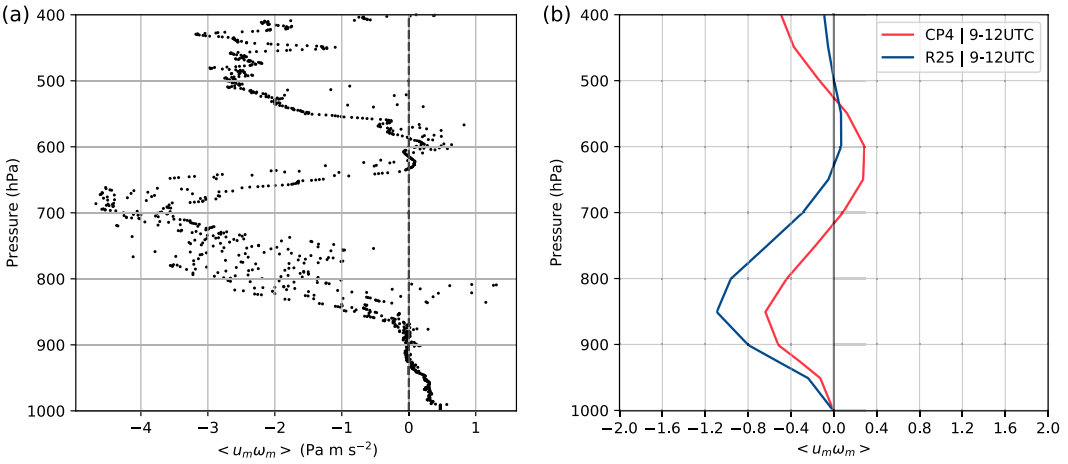

FIG. 10. (a) Vertical profile of convective momentum flux $\langle u_m\omega_m\rangle$ measured by the dropsondes in the JET2000 campaign at 11°N. (b) Vertical profile of convective momentum flux $\langle u_m\omega_m\rangle$ calculated using storm-relative winds from composites around grid cells precipitating at a rate of 1 mm h^{-1} or greater at 0900–1200 UTC in CP4 (red line) and R25 (blue line).

Note that the scales are different for observed (Fig. 9a) and modeled (Figs. 9b,c) plots since composited fields are a mean representation of many events, so it is difficult to compare the intensity of the vorticity signatures. Above 800 hPa, the shape of the observed signature is closer to the dipole structure in CP4 than the single positive vorticity anomaly in R25. Below 800 hPa, the observed reversed vorticity dipole is not present in either simulation. This signature may be a feature of decaying storms specifically, or perhaps is located only in the stratiform region, which is not uniquely sampled by the compositing method. There is evidence for the latter: while not present in Figs. 9b and 9c, composites centered two grid cells to the west of precipitating grid cells (not shown) show low level divergence that matches the observations.

Few studies provide detailed observations of the internal structure of Sahelian storms. One of the few examples is a squall line observed on 22 June 1981 as part of the COPT81 project, analyzed in Chong et al. (1987), Roux (1988), and Chalon et al. (1988). These papers show AEJ deceleration after the squall line passes, consistent with the observed vorticity structure in this paper, and describe the descending rear inflow jet that eventually reaches the surface. We can see a rear inflow jet in plots of zonal velocity (not shown).

The dropsonde observations were also used to calculate an approximation of convective momentum flux $\langle u_m\omega_m\rangle$ up to 400 hPa, shown in Fig. 10a. Measurements of zonal wind were used to calculate u_m at 11°N. The ω_m was calculated by integrating

$$\frac{\partial\omega}{\partial p} = -\frac{\partial u}{\partial x} - \frac{\partial v}{\partial y}$$

with respect to pressure. No data were available to calculate $\partial u/\partial x$, but a descending easterly rear inflow jet would contribute a negative $\partial u/\partial x$ at midlevels and above in the stratiform region of the storm behind the convective line. The $\partial\omega/\partial p$ term may, therefore, be more positive than our estimate, which would lead to a quicker decrease in omega with height, thus a shortened downdraft, and hence a more pronounced positive omega anomaly at 600 hPa.

Figure 10a shows a similar vertical structure to modeled profiles of $\langle u_m\omega_m\rangle$ in Fig. 10b, with a stronger negative anomaly at lower levels and a weaker positive anomaly that peaks at around 650 hPa, and the correction discussed in the previous paragraph would bring the structure closer to the modeled ratio of peaks in CP4. The positive anomaly occurs in the region where the vertical velocity has become an updraft but the AEJ still causes a negative zonal velocity anomaly, leading to a positive product. Physically the anomaly corresponds to the upward transport of easterly momentum from the jet.

The maximum negative momentum transport is smaller in both simulations' composites than in the observed storm, which may again be the dilution effect of composites. The peak is also at a lower height in the simulations than the observations, perhaps because MCSs tend to have a descending rear inflow jet and at this point behind the storm, the rear inflow jet is higher than it might be as it approaches the leading edge of the storm. Therefore, the zonal wind profile of the observation will be elevated and as such so will the convective momentum signature. Although a comparison with a single observation is not a robust validation, CP4 does reflect convective momentum transport more similarly to the observed case.

5. Conclusions

In this paper, we consider connections between processes on meso- and synoptic scales in a specific focus area (Fig. 2) using two regional current-climate simulations: one with a deep convection parameterization and one without. Following Haynes and McIntyre (1987), we calculate a synoptic circulation budget with terms split by separating both vorticity and velocity into their diurnal mean ("synoptic") and perturbation ("anomalous") components. We composite dynamical quantities

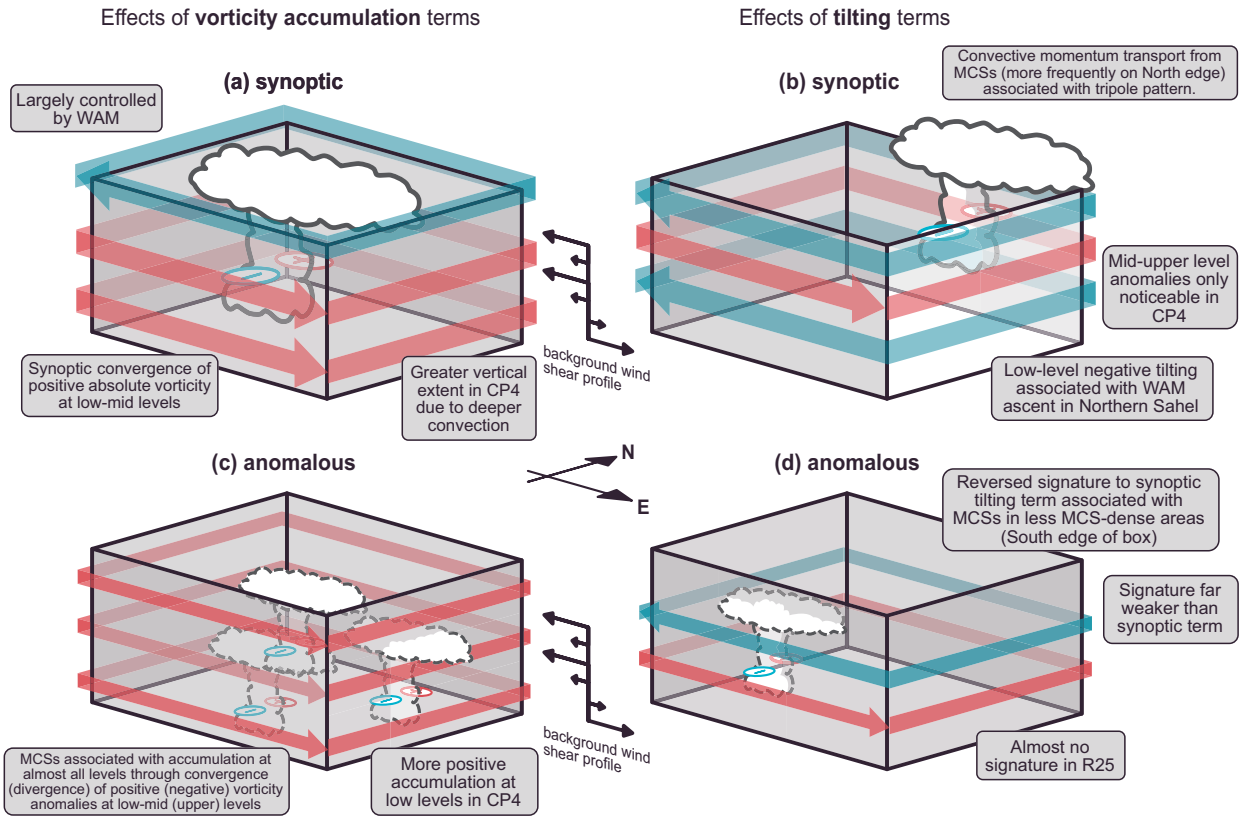

FIG. 11. Schematic illustrating the effects of (a),(c) vorticity accumulation and (b),(d) vortex tilting linked to convection on the circulation budget, showing (top) synoptic (diurnal mean) effects and (bottom) anomalous effects. Storms are illustrated in the location in the box where they impact this term, with larger storms indicating the more frequent location of precipitating pixels and smaller storms indicating more anomalous precipitating features. Red and blue arrows indicate reinforcement of cyclonic and anticyclonic circulation, respectively. Objects, and illustrative arrows, are not to scale.

corresponding to the accumulation and tilting terms in the circulation budget around precipitating grid cells to build up a picture of the dynamics of a typical MCS, and link these processes to the circulation tendencies in the region, highlighting the relevance of convective momentum transport to the tilting term. Last, we compare simulated precipitating systems with an observational case from the JET2000 field campaign in August of 2000.

The contributions of convection-related processes in the four circulation budget terms we consider, and their differences between the two simulations, are outlined in the schematic shown in Fig. 11. The circulation budget is dominated by the "synoptic accumulation" term (Fig. 11a), which is reasonably similar between the two simulations except for a slight difference in diurnal timing that corresponds to a lag in rainfall peak, and vertical extent. A process-based analysis explains that the WAM largely drives synoptic accumulation, but convective systems play a role in reinforcing and disrupting the WAM's diurnal variation. Storms contained entirely within a circulation will cause convergence of positive vorticity anomalies at lower levels, and at midlevels where there is substantial elevated convection, resulting in positive accumulation anomalies that move upward as convection becomes more elevated overnight. At upper levels, storms cause divergence of positive background vorticity, resulting in negative accumulation anomalies on the synoptic scale. In CP4, since convection is deeper and more intense, stronger updrafts mean that more negative vorticity anomalies are generated at upper levels, which lower the overall mean positive vorticity, reducing the magnitude of negative synoptic accumulation term at this height. The greater vertical extent of convection in CP4 may be linked to the tendency of convection-permitting models to overestimate updraft speed and extent (Kendon et al. 2021). It is reassuring that the dominant term in the circulation budget, which appears to rely on convergence (and hence heating) profiles of convection, is similar in both simulations. It is not a new argument that the heating profile a parameterization produces is crucial for simulating the wider impacts of convective dynamics, but the work carried out in this paper supports the existing literature.

The representation of convection also affects the anomalous accumulation term, with the positive anomalies overnight representing the impacts of individual MCSs that do not occur in the same place regularly, but when they do initiate, their profile of vorticity accumulation is almost entirely positive (Fig. 5). The anomalous MCSs act to reinforce cyclonic circulation around them (Fig. 11c).

The greatest differences between the two simulations' circulation budgets are in the synoptic tilting term. We suggest

that diurnal convection projects onto the synoptic tilting term, and is the most likely explanation of the difference in the term between simulations at mid- to upper levels. This term is linked to convective momentum transport, a relationship detailed in section 4b and the appendix. Both simulations indicate an intense negative anomaly at low levels in composites of the integrand of the tilting term, so storms on the eastern or northern edges of a cyclonic circulation will accelerate cyclonic circulation and, conversely, storms on the western or southern edges of a cyclonic circulation will decelerate cyclonic circulation, between approximately 900 and 600 hPa. In CP4, there is an opposite effect at 600–400 hPa, and it returns to the original pattern above 400 hPa. The synoptic tilting term in CP4 shows a corresponding pattern, indicating that storm-scale momentum transport can modulate circulation on a large scale in simulations with resolved convection (Fig. 11b). Anomalous tilting shows a signature with opposing signs, indicating that some storms contribute an opposing circulation tendency to the diurnal pattern of rainfall: these are the less-frequent storms on the southern side of the box in CP4 and on the northern side of the box in R25 (Fig. 11d).

CP4's convincingly narrow vorticity dipole and convergence profile around mesoscale precipitation suggest it is more similar to an observed storm than R25. However, CP4's vorticity anomalies are not quite narrow enough and its peak in convective momentum transport is at too low a height. A single observation does not provide a perfect comparison with reality, so we cannot draw reliable conclusions about which simulation is more realistic.

Our analysis focuses on a fixed region, but understanding could be applied to specific case studies of circulations such as AEWs. There is a consensus in the literature on the collocation of convection with the front of an AEW trough, reinforcing the AEW circulation (see section 1). Our results indicate that the momentum transport on the southern edge of a vortex serves to reinforce it, despite literature suggesting that weaker (nondeveloping) AEWs have convection to their south. However, convection on the western edge of a trough would reinforce the low-level cyclonic circulation associated with an AEW: that is, at the front of an AEW trough, consistent with the literature.

In summary, this paper reaffirms the importance of simulating realistic heating profiles in convective parameterizations. It further illuminates the less crucial but still relevant role of considering convective momentum transport in MCSs, which in this particular case was distinctly different between simulations with and without a deep convection parameterization. Convective momentum transport is therefore an important factor to consider in developing parameterizations in the future.

Acknowledgments. This work was supported by the Leeds–York–Hull Natural Environment Research Council (NERC) Doctoral Training Partnership (DTP) Panorama under Grant NE/S007458/1. This work was also supported by Global Challenges Research Fund (GCRF) African SWIFT, Grant/Award Number NE/P021077/1. Data from the JET2000 field campaign (Grant NER/A/S/1999/00092) as part of AMMA-2050 (Grant NE/M020126/1) were used, as well as data produced as an output of IMPALA (NE/M017176/1). The authors thank three reviewers for excellent constructive and helpful feedback on the paper.

Data availability statement. A sample of data from FCFA IMPALA's present-day CP4 dataset can be accessed via the CEDA Data Archive (https://catalogue.ceda.ac.uk/uuid/f46b14e670fc49cbaadf108c969e7ee0). Guidelines for accessing the data can be found in the CP4-Africa Technical Guidelines (Senior et al. 2020). Data from JET2000 flight A781 are open access and can be downloaded from the CEDA Data Archive (https://catalogue.ceda.ac.uk/uuid/b4e1cf1f398045d3ab253a5c22044892; Met Office and Parker 2006).

APPENDIX

The Flux-Form Vorticity and Momentum Equations

The flux-form vorticity equation is outlined in Eq. (1). To understand the link between the tilting term and the momentum flux, consider the flux form of the momentum equation:

$$\frac{\partial \mathbf{u}}{\partial t} + \nabla \cdot (\mathbf{uu}) = -f\hat{\mathbf{k}} \times \mathbf{u} - \nabla p - g\hat{\mathbf{k}}. \tag{A1}$$

Equation (A1) is a way of writing the Navier–Stokes equations for an incompressible fluid on a beta plane, neglecting viscous effects and assuming a constant gravitational force, where f is the Coriolis parameter, g is the gravitational field strength, p is the pressure, and $\mathbf{uu}$ is the momentum flux tensor, a tensor product of three-dimensional wind vector $\mathbf{u}$ with itself. Tensor $\mathbf{uu}$ can be explicitly written as

$$\mathbf{uu} = \begin{pmatrix} uu & uv & u\omega \\ uv & vv & v\omega \\ u\omega & v\omega & \omega\omega \end{pmatrix}. \tag{A2}$$

The momentum flux Λ described in Moncrieff (1992) is proportional to uw (or, in pressure coordinates, $u\omega$), which is one of the components of the momentum flux tensor (bottom row of the matrix). Considering this component only, we can calculate its pressure derivative $\partial \mathbf{u}\omega/\partial p$, which is one of the terms of the divergence of the momentum flux tensor $\nabla \cdot (\mathbf{uu})$ and is proportional to momentum change $\partial \mathbf{u}/\partial t$. Since

$$\frac{\partial}{\partial p}(\mathbf{u}\omega) = \mathbf{u}\frac{\partial \omega}{\partial p} + \omega\frac{\partial \mathbf{u}}{\partial p}, \tag{A3}$$

we see that the variation of the momentum flux Λ is indeed controlled to some extent by the "tilting" term $\omega(\partial \mathbf{u}/\partial p)$.

REFERENCES

Alfaro, D. A., 2017: Low-tropospheric shear in the structure of squall lines: Impacts on latent heating under layer-lifting ascent. *J. Atmos. Sci.*, **74**, 229–248, https://doi.org/10.1175/JAS-D-16-0168.1.

Badlan, R. L., T. P. Lane, M. W. Moncrieff, and C. Jakob, 2017: Insights into convective momentum transport and its parametrization

from idealized simulations of organized convection. *Quart. J. Roy. Meteor. Soc.*, **143**, 2687–2702, https://doi.org/10.1002/qj.3118.

Baidu, M., J. Schwendike, J. H. Marsham, and C. Bain, 2022: Effects of vertical wind shear on intensities of mesoscale convective systems over west and central Africa. *Atmos. Sci. Lett.*, **23**, e1094, https://doi.org/10.1002/asl.1094.

Berry, G. J., and C. Thorncroft, 2005: Case study of an intense African easterly wave. *Mon. Wea. Rev.*, **133**, 752–766, https://doi.org/10.1175/MWR2884.1.

Berthou, S., D. P. Rowell, E. J. Kendon, M. J. Roberts, R. A. Stratton, J. A. Crook, and C. Wilcox, 2019: Improved climatological precipitation characteristics over West Africa at convection-permitting scales. *Climate Dyn.*, **53**, 1991–2011, https://doi.org/10.1007/s00382-019-04759-4.

Bickle, M. E., J. H. Marsham, A. N. Ross, D. P. Rowell, D. J. Parker, and C. M. Taylor, 2021: Understanding mechanisms for trends in Sahelian squall lines: Roles of thermodynamics and shear. *Quart. J. Roy. Meteor. Soc.*, **147**, 983–1006, https://doi.org/10.1002/qj.3955.

Birch, C. E., J. H. Marsham, D. J. Parker, and C. M. Taylor, 2014a: The scale dependence and structure of convergence fields preceding the initiation of deep convection. *Geophys. Res. Lett.*, **41**, 4769–4776, https://doi.org/10.1002/2014GL060493.

——, D. J. Parker, J. H. Marsham, D. Copsey, and L. Garcia-Carreras, 2014b: A seamless assessment of the role of convection in the water cycle of the West African monsoon. *J. Geophys. Res. Atmos.*, **119**, 2890–2912, https://doi.org/10.1002/2013JD020887.

Boutle, I. A., J. E. J. Eyre, and A. P. Lock, 2014: Seamless stratocumulus simulation across the turbulent gray zone. *Mon. Wea. Rev.*, **142**, 1655–1668, https://doi.org/10.1175/MWR-D-13-00229.1.

Chalon, J. P., G. Jaubert, J. P. Lafore, and F. Roux, 1988: The West African squall line observed on 23 June 1981 during COPT 81: Mesoscale structure and transports. *J. Atmos. Sci.*, **45**, 2744–2763, https://doi.org/10.1175/1520-0469(1988)045<2744:TWASLO>2.0.CO;2.

Chong, M., P. Amayenc, G. Scialom, and J. Testud, 1987: A tropical squall line observed during the COPT 81 experiment in West Africa. Part 1: Kinematic structure inferred from dual-Doppler radar data. *Mon. Wea. Rev.*, **115**, 670–694, https://doi.org/10.1175/1520-0493(1987)115<0670:ATSLOD>2.0.CO;2.

Crook, J., C. Klein, S. Folwell, C. M. Taylor, D. J. Parker, R. Stratton, and T. Stein, 2019: Assessment of the representation of West African storm lifecycles in convection-permitting simulations. *Earth Space Sci.*, **6**, 818–835, https://doi.org/10.1029/2018EA000491.

Dickinson, M., and J. Molinari, 2000: Climatology of sign reversals of the meridional potential vorticity gradient over Africa and Australia. *Mon. Wea. Rev.*, **128**, 3890–3900, https://doi.org/10.1175/1520-0493(2001)129<3890:COSROT>2.0.CO;2.

Diongue, A., J.-P. Lafore, J.-L. Redelsperger, and R. Roca, 2002: Numerical study of a Sahelian synoptic weather system: Initiation and mature stages of convection and its interactions with the large-scale dynamics. *Quart. J. Roy. Meteor. Soc.*, **128**, 1899–1927, https://doi.org/10.1256/003590002320603467.

Dosio, A., R. G. Jones, C. Jack, C. Lennard, G. Nikulin, and B. Hewitson, 2019: What can we know about future precipitation in Africa? Robustness, significance and added value of projections from a large ensemble of regional climate models. *Climate Dyn.*, **53**, 5833–5858, https://doi.org/10.1007/s00382-019-04900-3.

Eliassen, A., 1983: The Charney-Stern theorem on barotropic-baroclinic instability. *Pure Appl. Geophys.*, **121**, 563–572, https://doi.org/10.1007/BF02590155.

Elless, T. J., and R. D. Torn, 2018: African easterly wave forecast verification and its relation to convective errors within the ECMWF Ensemble Prediction System. *Wea. Forecasting*, **33**, 461–477, https://doi.org/10.1175/WAF-D-17-0130.1.

Fink, A. H., and Coauthors, 2017: Mean climate and seasonal cycle. *Meteorology of Tropical West Africa*, John Wiley and Sons, 452–468, https://doi.org/10.1002/9781118391297.ch1.

Fitzpatrick, R. G. J., and Coauthors, 2020: What drives the intensification of mesoscale convective systems over the West African Sahel under climate change? *J. Climate*, **33**, 3151–3172, https://doi.org/10.1175/JCLI-D-19-0380.1.

Haynes, P. H., and M. E. McIntyre, 1987: On the evolution of vorticity and potential vorticity in the presence of diabatic heating and frictional or other forces. *J. Atmos. Sci.*, **44**, 828–841, https://doi.org/10.1175/1520-0469(1987)044<0828:OTEOVA>2.0.CO;2.

Holton, J. R., 2004: Mesoscale circulations. *An Introduction to Dynamic Meteorology*, J. R. Holton, Ed., International Geophysics Series, Vol. 88, Academic Press, 268–312, https://doi.org/10.1016/S0074-6142(04)80043-3.

Hsieh, J.-S., and K. H. Cook, 2005: Generation of African easterly wave disturbances: Relationship to the African easterly jet. *Mon. Wea. Rev.*, **133**, 1311–1327, https://doi.org/10.1175/MWR2916.1.

——, and ——, 2008: On the instability of the African easterly jet and the generation of African waves: Reversals of the potential vorticity gradient. *J. Atmos. Sci.*, **65**, 2130–2151, https://doi.org/10.1175/2007JAS2552.1.

Jackson, L. S., J. H. Marsham, D. J. Parker, D. L. Finney, R. G. J. Fitzpatrick, D. P. Rowell, R. A. Stratton, and S. Tucker, 2022: The effect of explicit convection on climate change in the West African monsoon and central West African Sahel rainfall. *J. Climate*, **35**, 1537–1557, https://doi.org/10.1175/JCLI-D-21-0258.1.

Kendon, E. J., R. Stratton, S. Tucker, J. Marsham, S. Berthou, D. Rowell, and C. Senior, 2019: Enhanced future changes in wet and dry extremes over Africa at convection-permitting scale. *Nat. Commun.*, **10**, 1794, https://doi.org/10.1038/s41467-019-09776-9.

——, A. F. Prein, C. A. Senior, and A. Stirling, 2021: Challenges and outlook for convection-permitting climate modelling. *Philos. Trans. Roy. Soc.*, **A379**, 20190547, https://doi.org/10.1098/rsta.2019.0547.

Khouider, B., and A. J. Majda, 2006: A simple multicloud parameterization for convectively coupled tropical waves. Part I: Linear analysis. *J. Atmos. Sci.*, **63**, 1308–1323, https://doi.org/10.1175/JAS3677.1.

Klein, C., F. Nkrumah, C. M. Taylor, and E. A. Adefisan, 2021: Seasonality and trends of drivers of mesoscale convective systems in southern West Africa. *J. Climate*, **34**, 71–87, https://doi.org/10.1175/JCLI-D-20-0194.1.

Kuang, Z., 2008: A moisture-stratiform instability for convectively coupled waves. *J. Atmos. Sci.*, **65**, 834–854, https://doi.org/10.1175/2007JAS2444.1.

Lock, A. P., A. R. Brown, M. R. Bush, G. M. Martin, and R. N. B. Smith, 2000: A new boundary layer mixing scheme. Part I: Scheme description and single-column model tests. *Mon. Wea. Rev.*, **128**, 3187–3199, https://doi.org/10.1175/1520-0493(2000)128<3187:ANBLMS>2.0.CO;2.

Mapes, B. E., 2000: Convective inhibition, subgrid-scale triggering energy, and stratiform instability in a toy tropical wave model. *J. Atmos. Sci.*, **57**, 1515–1535, https://doi.org/10.1175/1520-0469(2000)057<1515:CISSTE>2.0.CO;2.

Marsham, J. H., N. S. Dixon, L. Garcia-Carreras, G. M. S. Lister, D. J. Parker, P. Knippertz, and C. E. Birch, 2013: The role of moist convection in the West African monsoon system: Insights from continental-scale convection-permitting simulations. *Geophys. Res. Lett.*, **40**, 1843–1849, https://doi.org/10.1002/grl.50347.

Mathon, V., H. Laurent, and T. Lebel, 2002: Mesoscale convective system rainfall in the Sahel. *J. Appl. Meteor.*, **41**, 1081–1092, https://doi.org/10.1175/1520-0450(2002)041<1081:MCSRIT>2.0.CO;2.

Mekonnen, A., C. D. Thorncroft, and A. R. Aiyyer, 2006: Analysis of convection and its association with African easterly waves. *J. Climate*, **19**, 5405–5421, https://doi.org/10.1175/JCLI3920.1.

Met Office, and D. J. Parker, 2006: MRF A781 JET2000 flight: Airborne atmospheric and chemistry measurements taken on board the Met Office C-130 Hercules aircraft. NCAS British Atmospheric Data Centre, accessed 25 March 2024, https://catalogue.ceda.ac.uk/uuid/b4e1cf1f398045d3ab253a5c22044892.

Moncrieff, M. W., 1992: Organized convective systems: Archetypal dynamical models, mass and momentum flux theory, and parametrization. *Quart. J. Roy. Meteor. Soc.*, **118**, 819–850, https://doi.org/10.1002/qj.49711850703.

——, C. Liu, and P. Bogenschutz, 2017: Simulation, modeling, and dynamically based parameterization of organized tropical convection for global climate models. *J. Atmos. Sci.*, **74**, 1363–1380, https://doi.org/10.1175/JAS-D-16-0166.1.

Moore, R. W., and M. T. Montgomery, 2005: Analysis of an idealized, three-dimensional diabatic Rossby vortex: A coherent structure of the moist baroclinic atmosphere. *J. Atmos. Sci.*, **62**, 2703–2725, https://doi.org/10.1175/JAS3472.1.

Núñez Ocasio, K. M., J. L. Evans, and G. S. Young, 2020: A wave-relative framework analysis of AEW–MCS interactions leading to tropical cyclogenesis. *Mon. Wea. Rev.*, **148**, 4657–4671, https://doi.org/10.1175/MWR-D-20-0152.1.

Pante, G., and P. Knippertz, 2019: Resolving Sahelian thunderstorms improves mid-latitude weather forecasts. *Nat. Commun.*, **10**, 3487, https://doi.org/10.1038/s41467-019-11081-4.

Panthou, G., T. Vischel, T. Lebel, J. Blanchet, G. Quantin, and A. Ali, 2012: Extreme rainfall in West Africa: A regional modeling. *Water Resour. Res.*, **48**, W08501, https://doi.org/10.1029/2012WR012052.

——, and Coauthors, 2018: Rainfall intensification in tropical semi-arid regions: The Sahelian case. *Environ. Res. Lett.*, **13**, 064013, https://doi.org/10.1088/1748-9326/aac334.

Parker, D. J., and A. J. Thorpe, 1995: Conditional convective heating in a baroclinic atmosphere: A model of convective frontogenesis. *J. Atmos. Sci.*, **52**, https://doi.org/10.1175/1520-0469(1995)052<1699:CCHIAB>2.0.CO;2.

——, C. D. Thorncroft, R. R. Burton, and A. Diongue-Niang, 2005a: Analysis of the African easterly jet, using aircraft observations from the JET2000 experiment. *Quart. J. Roy. Meteor. Soc.*, **131**, 1461–1482, https://doi.org/10.1256/qj.03.189.

——, and Coauthors, 2005b: The diurnal cycle of the West African monsoon circulation. *Quart. J. Roy. Meteor. Soc.*, **131**, 2839–2860, https://doi.org/10.1256/qj.04.52.

Parsons, D. B., S. P. Lillo, C. P. Rattray, P. Bechtold, M. J. Rodwell, and C. M. Bruce, 2019: The role of continental mesoscale convective systems in forecast busts within global weather prediction systems. *Atmosphere*, **10**, 681, https://doi.org/10.3390/atmos10110681.

Pearson, K. J., R. J. Hogan, R. P. Allan, G. M. S. Lister, and C. E. Holloway, 2010: Evaluation of the model representation of the evolution of convective systems using satellite observations of outgoing longwave radiation. *J. Geophys. Res.*, **115**, D20206, https://doi.org/10.1029/2010JD014265.

Peters, K., C. Hohenegger, and D. Klocke, 2019: Different representation of mesoscale convective systems in convection-permitting and convection-parameterizing NWP models and its implications for large-scale forecast evolution. *Atmosphere*, **10**, 503, https://doi.org/10.3390/atmos10090503.

Pytharoulis, I., and C. Thorncroft, 1999: The low-level structure of African easterly waves in 1995. *Mon. Wea. Rev.*, **127**, 2266–2280, https://doi.org/10.1175/1520-0493(1999)127<2266:TLLSOA>2.0.CO;2.

Raymond, D. J., and S. L. Sessions, 2014: Tropical cyclogenesis and mid-level vorticity. *Aust. Meteor. Oceanogr. J.*, **64**, 11–25, https://doi.org/10.22499/2.6401.003.

Rotunno, R., J. B. Klemp, and M. L. Weisman, 1988: A theory for strong, long-lived squall lines. *J. Atmos. Sci.*, **45**, 463–485, https://doi.org/10.1175/1520-0469(1988)045<0463:ATFSLL>2.0.CO;2.

Roux, F., 1988: The West African squall line observed on 23 June 1981 during COPT 81: Kinematics and thermodynamics of the convective region. *J. Atmos. Sci.*, **45**, 406–426, https://doi.org/10.1175/1520-0469(1988)045<0406:TWASLO>2.0.CO;2.

Rowell, D. P., C. A. Senior, M. Vellinga, and R. J. Graham, 2016: Can climate projection uncertainty be constrained over Africa using metrics of contemporary performance? *Climatic Change*, **134**, 621–633, https://doi.org/10.1007/s10584-015-1554-4.

Russell, J. O. H., A. Aiyyer, and J. D. White, 2020: African easterly wave dynamics in convection-permitting simulations: Rotational stratiform instability as a conceptual model. *J. Adv. Model. Earth Syst.*, **12**, e2019MS001706, https://doi.org/10.1029/2019MS001706.

Schubert, W. H., P. E. Ciesielski, D. E. Stevens, and H.-C. Kuo, 1991: Potential vorticity modeling of the ITCZ and the Hadley circulation. *J. Atmos. Sci.*, **48**, 1493–1509, https://doi.org/10.1175/1520-0469(1991)048<1493:PVMOTI>2.0.CO;2.

Senior, C., and Coauthors, 2020: Technical guidelines for using CP4-Africa simulation data. Zenodo, https://doi.org/10.5281/zenodo.4316467.

Smagorinsky, J., 1963: General circulation experiments with the primitive equations: I. The basic experiment. *Mon. Wea. Rev.*, **91**, 99–164, https://doi.org/10.1175/1520-0493(1963)091<0099:GCEWTP>2.3.CO;2.

Smith, R. N. B., 1990: A scheme for predicting layer clouds and their water content in a general circulation model. *Quart. J. Roy. Meteor. Soc.*, **116**, 435–460, https://doi.org/10.1002/qj.49711649210.

Stevens, B., and S. Bony, 2013: What are climate models missing? *Science*, **340**, 1053–1054, https://doi.org/10.1126/science.1237554.

Stratton, R. A., and Coauthors, 2018: A pan-African convection-permitting regional climate simulation with the Met Office Unified Model: CP4-Africa. *J. Climate*, **31**, 3485–3508, https://doi.org/10.1175/JCLI-D-17-0503.1.

Taylor, C. M., C. E. Birch, D. J. Parker, N. Dixon, F. Guichard, G. Nikulin, and G. M. S. Lister, 2013: Modeling soil moisture-precipitation feedback in the Sahel: Importance of spatial scale versus convective parameterization. *Geophys. Res. Lett.*, **40**, 6213–6218, https://doi.org/10.1002/2013GL058511.

——, and Coauthors, 2017: Frequency of extreme Sahelian storms tripled since 1982 in satellite observations. *Nature*, **544**, 475–478, https://doi.org/10.1038/nature22069.

Thorncroft, C. D., and M. Blackburn, 1999: Maintenance of the African easterly jet. *Quart. J. Roy. Meteor. Soc.*, **125**, 763–786, https://doi.org/10.1002/qj.49712555502.

——, and Coauthors, 2003: The JET2000 project: Aircraft observations of the African easterly jet and African easterly waves. *Bull. Amer. Meteor. Soc.*, **84**, 337–352, https://doi.org/10.1175/BAMS-84-3-337.

——, N. M. J. Hall, and G. N. Kiladis, 2008: Three-dimensional structure and dynamics of African easterly waves. Part III: Genesis. *J. Atmos. Sci.*, **65**, 3596–3607, https://doi.org/10.1175/2008JAS2575.1.

Tomassini, L., 2018: Mesoscale circulations and organized convection in African easterly waves. *J. Atmos. Sci.*, **75**, 4357–4381, https://doi.org/10.1175/JAS-D-18-0183.1.

Vizy, E. K., and K. H. Cook, 2018: Mesoscale convective systems and nocturnal rainfall over the West African Sahel: Role of the inter-tropical front. *Climate Dyn.*, **50**, 587–614, https://doi.org/10.1007/s00382-017-3628-7.

Walters, D., and Coauthors, 2019: The Met Office Unified Model Global Atmosphere 7.0/7.1 and JULES Global Land 7.0 configurations. *Geosci. Model Dev.*, **12**, 1909–1963, https://doi.org/10.5194/gmd-12-1909-2019.

Wilson, D. R., and S. P. Ballard, 1999: A microphysically based precipitation scheme for the UK Meteorological Office Unified Model. *Quart. J. Roy. Meteor. Soc.*, **125**, 1607–1636, https://doi.org/10.1002/qj.49712555707.

——, A. C. Bushell, A. M. Kerr-Munslow, J. D. Price, and C. J. Morcrette, 2008: PC2: A prognostic cloud fraction and condensation scheme. I: Scheme description. *Quart. J. Roy. Meteor. Soc.*, **134**, 2093–2107, https://doi.org/10.1002/qj.333.

Wu, M.-L. C., O. Reale, S. D. Schubert, M. J. Suarez, R. D. Koster, and P. J. Pegion, 2009: African easterly jet: Structure and maintenance. *J. Climate*, **22**, 4459–4480, https://doi.org/10.1175/2009JCLI2584.1.

Zipser, E. J., D. J. Cecil, C. Liu, S. W. Nesbitt, and D. P. Yorty, 2006: Where are the most intense thunderstorms on Earth? *Bull. Amer. Meteor. Soc.*, **87**, 1057–1072, https://doi.org/10.1175/BAMS-87-8-1057.